

# Composite of Tin and Silicon with Nanostructure as High Performance Lithium-Ion Battery Anode

Chao Wang, Xiufang Bian\*, Yinghui Yang, Chao Yuan, Junzhang Wang, Mengchun Yu, Rongzhang Guan, Dujiang Lu

Key Laboratory for Liquid-Solid Structural Evolution and Processing of Materials, Ministry of Education, Shandong University, Jinan 250061, China

\*E-mail: [xfbian@sdu.edu.cn](mailto:xfbian@sdu.edu.cn)

Received: 7 December 2019 / Accepted: 13 February 2020 / Published: 10 March 2020

Composite of nanobranches-Si and nanospheres-Sn (denoted as Sn<sup>#</sup>nb-Si) with an appearance of “fruit-branch” is successfully synthesized by two-step method at room-temperature. This two-step method, i.e. dealloying followed by depositing, constructs an intact network of nanobranches-Si (nb-Si) with a harmonious depositing of nanospheres-Sn. The structural design at the nanoscale level buffers the expansion during lithiation/delithiation process, and the depositing of nanospheres-Sn improves the rate of Li<sup>+</sup> transfer (an increase of 145% compared to pure nb-Si), remedying inherent poor conductivity of Si and achieving enhanced electrochemical performance. As a result, Sn<sup>#</sup>nb-Si exhibits a reversible capacity of 1525.9 mA h g<sup>-1</sup> at 100 mA g<sup>-1</sup> after 55 cycles with decent rate performance. Furthermore, Sn<sup>#</sup>nb-Si deepens research on the composite of Si and Sn, while dealloying followed by depositing, which is generally facile and uncomplicated, offers a novel guideline to cultivate structural design and paves the way for the synthesis of advanced energy storage materials.

**Keywords:** LIBs, Si/Sn, anode, composite, dealloying, depositing

## 1. INTRODUCTION

Since the 1990s, research on lithium-ion batteries (LIBs) has flourished around the world, including research on electrode materials (anode[1-4] & cathode[5-6]), separator[7-8] and electrolyte[9-10]. The ever-increasing requirement for high-efficiency and high energy storage, of which anode is an example, entails research which manages to manufacture anode materials meeting such a requirement with low cost, environmental friendliness and large-scale application[11].

Silicon (Si) has been identified as an alternative anode material for LIBs of the next generation[12]. Different from carbon (C), which forms LiC<sub>6</sub> during lithiation by intercalation, Si can react with a much greater amount of Lithium through the alloying process, resulting in the ultrahigh

theoretical capacity of Si ( $4200 \text{ mA h g}^{-1}$ )[12]. However, a violent volume expansion as high as 400% affects Si significantly during the lithiation/delithiation process, leading to the destruction of the electrode and the fading of its reversible capacity[13]. Moreover, a shortage of electron conductivity and  $\text{Li}^+$  diffusivity limits Si to store more  $\text{Li}^+$  at a high current density, resulting in a poor rate performance[14-15]. Directly substituting bulk Si for C as an anode material results in an unsatisfactory performance.

Hence, aiming to advance the performance of Si, researchers around the world have attempted to modify such an attractive substitution. Forming an ordered structure at the nanoscale level helps solve the problem above, and a series of studies have been carried out over the last few decades, producing nanoporous Si[16], nanowires Si[17], nanosheets Si[18], nanotubes Si[10], and hollow porous Si[19]. Si with nanostructure has a large specific surface area, which supplies many more sites to react with  $\text{Li}^+$ . This benefits the contact between Si and the electrolyte, enhancing the ability of electron conductivity and  $\text{Li}^+$  diffusivity, alloying for fast charging/discharging[20-24]. Wang et al. reports that a binder-free electrode at the nanoscale level showed a fast charging performance, with a high specific capacity (over  $1200 \text{ mA h g}^{-1}$ ) at a current density of  $7C$ [3]. Additionally, the robustness of the ordered structure helps prevent the fiber from cracking, so that the effect of volume expansion can be diminished during the process of lithiation/delithiation[13,25]. For example, a nanoporous structure with ideal porosity can buffer the swell, thereby producing fewer fissures and averting the destruction of active materials. As a result, a robust solid electrolyte interface (SEI) forms, and the reversible capacity maintains its high level during the charging/discharging process[26-27].

Alongside the nanoscale Si, another strategy is composite[12,28]. Composites of Si and an advanced conductor can enhance performance, overcoming low diffusivity of  $\text{Li}^+$ [15]. Many binary materials have previously been studied, including Si-M binary composites such as Si-M (RGO[29], Mg[30], Ge[31], Sb[32], Fe[33], Sn[15,34-35]), showing the superiority of Si-base composites. In previous studies, our group has successfully synthesized 3D-NP SiGe and np-SiSb through dealloying, producing a favorable performance[31-32]. Furthermore, Sn coatings on silicon nanowire were studied by researchers through CVD growth and sputter coating[15]. It was found that structural design is not the only factor that determines the performance of active materials; proper coatings may induce a compressive stress during lithiation, thereby limiting the initiation of cracking[15]. Obviously, the ordered structural design of Sn holds the ability to strengthen both the structural stability of Si and its ionic diffusivity. However, Si/Sn composites with the same morphology do not always produce a good performance. Another study showed that tin-catalyzed silicon nanowires were synthesized with a result of  $1078 \text{ mA h g}^{-1}$  after 50 cycles, a poor performance compared to the ultrahigh capacity of Si[35]. It is apparent that composites of Si and Sn hold the potential to behave excellently in LIBs. This calls for brand-new strategies to synthesize Si/Sn composites in a facile way. Previous studies have not attempted a nanoscale Sn depositing of Si nanobranches necessitating the present research.

In this study, unlike Sn coatings on Si nanowires,  $\text{Sn}^{\#}\text{nb-Si}$  is synthesized through a two-step method, i.e. dealloying followed by depositing, both of which are facile and uncomplicated[36-37]. Sn nanospheres are deposited across the branches of the nanobranches-Si ligament, with the appearance of *sabina chinensis* and its fruit ball. Tested at a current density of  $100 \text{ mA g}^{-1}$ , reversible capacity of  $1525.9 \text{ mA h g}^{-1}$  still maintains after 55 cycles, suggesting that  $\text{Sn}^{\#}\text{nb-Si}$  has the potential to be applied large-

scale to advanced performance energy storage devices.

## 2. EXPERIMENTAL SECTION

### 2.1 Synthesis of Active Material

AlSi alloy was prepared by melting pure Al (99.999%) and pure Si (99.999%) in the corundum crucible using a high frequency induction heating furnace (1073 K for 8 min). After that, an iron chill mold was used to form an AlSi alloy ingot. AlSi ribbons were prepared by a single roller melt spinning apparatus (Model number: SP009 A). The ingot was remelted in an Ar-protected quartz tube by high frequency induction, and then the fusant was spun onto a copper roller at a linear velocity of  $\sim 27 \text{ m s}^{-1}$ . The prepared ribbons showed the color of silver and were  $\sim 3 \text{ mm}$  in width,  $\sim 35 \text{ }\mu\text{m}$  in thickness and several decimeters longitudinally.

The dealloying of the ribbons were proceeded in 5 wt% hydrochloric acid (HCl) at room temperature with constant magnetic stirring for 12 h until no more bubbles arose. The turbid substance was washed 3 times with deionized water and was then dried in a vacuum at 353 K for 12 h. Ethylene glycol ( $(\text{CH}_2\text{OH})_2$ ) was used to dissolve stannic chloride ( $\text{SnCl}_4$ ). Then, the as-prepared powders were immersed into a glycol solution, and a 15-min ultrasonic treatment ensured the equilibrium of the mixture. After that, sodium borohydride ( $\text{NaBH}_4$ ) was added slowly to react with  $\text{Sn}^{4+}$ , and simultaneously nanospheres Sn was deposited. The as-synthesized composite was centrifuged and washed with deionized water until no more acid-base property showed. Lastly, particles were dried in a vacuum at 353K for 10 h.

### 2.2 Materials Characterization

X-ray diffraction (XRD, Rigaku Dmax-rc diffractometer), Raman spectrocope (RENISHAW in Via), and X-ray photo-electron spectroscopy (XPS, AXIS Supra) were used to characterize the structure and ingredients of the synthesized samples. The microstructure of the samples was analyzed by a scanning electron microscope (SEM, Hitachi SU-70) attached to an X-ray energy dispersive spectrometre (EDS) and a transmission electron microscope (TEM, JEOL-2100F).  $\text{N}_2$  absorption/desorption isotherms were measured at 77.3 K by ASAP-2460 to characterize the porosity and surface area.

### 2.3 Electrochemical Measurements

2032 coin-type half-cells were assembled using the as-synthesized samples to test its electrochemical performance.

The samples were mixed with acetylene black and sodium carboxymethyl cellulose (CMC) at a ratio of 75:15:10 (wt%) in deionized water. Then, the viscous composite was loaded onto a Cu foil current collector, and then was dried in a vacuum at 353K for 8 h. Cu foil was cut in roundness with a

diameter of 14 mm to get the electrode. The half-coin cells were assembled in a glovebox full of argon (99.99%), while a pure Li sheet was used as the counter electrode, Celgard 2400 as separator, and 1 M  $\text{LiPF}_6$  with 1:1:1 (vol%) ethylene carbonate/dimethyl carbonate/diethyl carbonate as electrolyte. Galvanostatic discharge/charge cycles tests were performed on a channel battery cyler (Neware CT-4008, Shenzhen, China) between 0.01-1.5V. The cyclic voltammetry (CV) curve was performed in the voltage range of 0.01 to 3V (vs.  $\text{Li/Li}^+$ ) at a sweep rate of  $0.1 \text{ mV s}^{-1}$ . The electrochemical impedance spectroscopy (EIS) performance was measured on an electrochemical workstation (CHI 660E, Shanghai China) in a frequency range of 0.01 Hz - 100 kHz.

The electrode synthesis and the testing conditions of the control groups (np-SiSn, nb-Si and SiSn(NPs)) were the same as  $\text{Sn}^{\#}\text{nb-Si}$ .

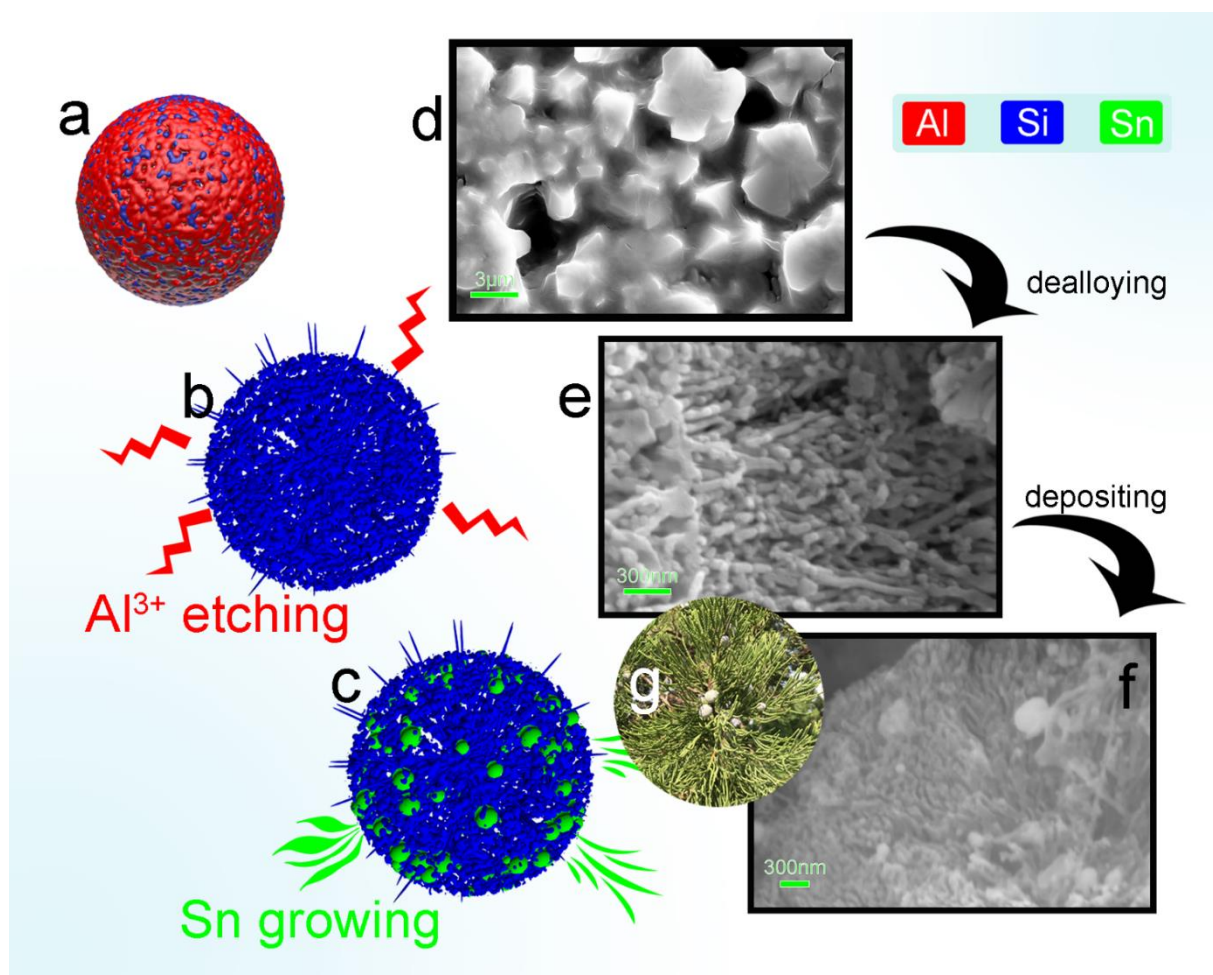


**Figure 1.** a-c, schematic of evolution of samples, a) AlSi alloy, b) nb-Si after chemical dealloying, c)  $\text{Sn}^{\#}\text{nb-Si}$  after depositing; d-f, SEM images of AlSi alloy, nb-Si and  $\text{Sn}^{\#}\text{nb-Si}$ , corresponding to a-c respectively; g) picture of *Sabina chinensis* with its fruit ball.

### 3. RESULTS AND DISCUSSION

Dealloying has been used for decades to fabricate three-dimensional nanoscale materials. In this process, the sacrificial elements are etched away, after which the organized structure with a dimension

of several nanometers remains. Depositing, due to its simplicity, has also been widely used as an advanced synthesis strategy to acquire composites[38]. Hence, an AlSi alloy was remelted and underwent an ultrahigh cooling rate, leading to constitutional and potentially beneficial changes in its solid phase. Al was selectively dissolved from the network and nb-Si remained after etching. After depositing, Sn nanospheres were deposited across the nanobranches Si.

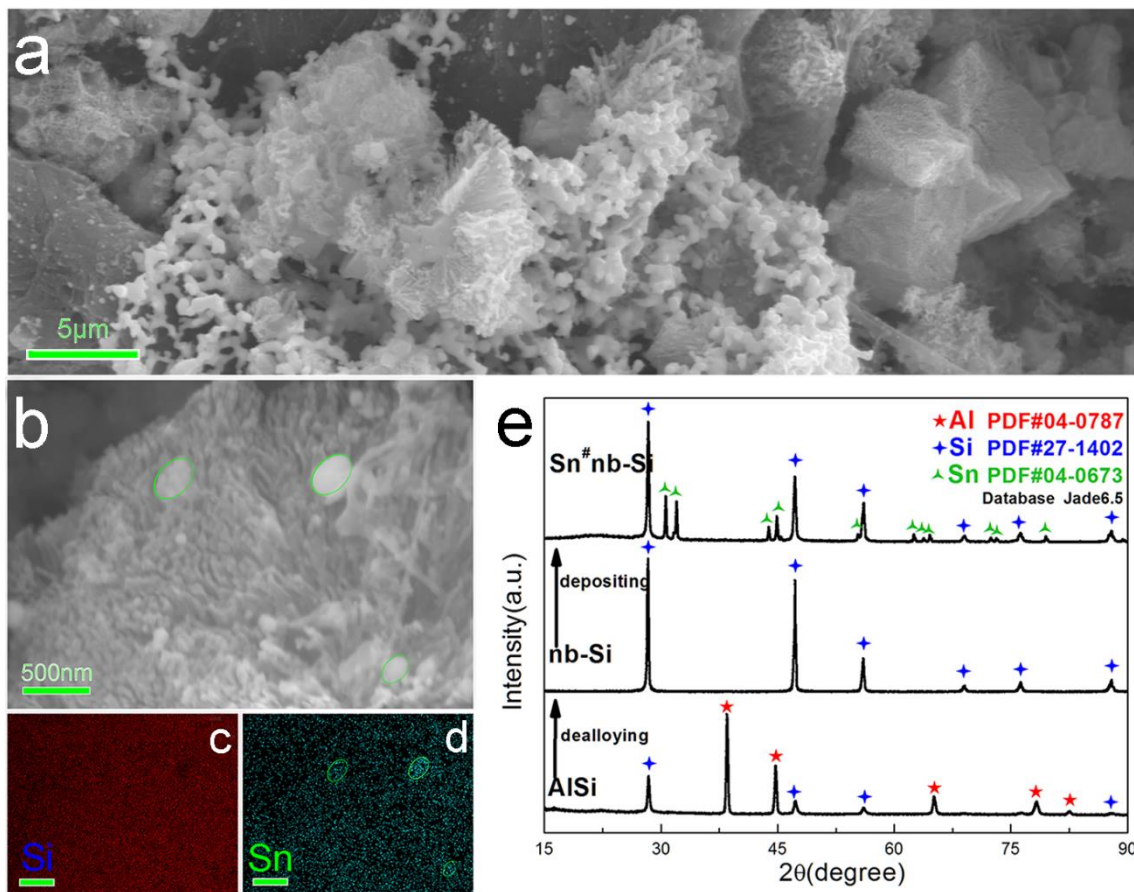


**Figure 2.** a) low-magnification SEM image of Sn<sup>#</sup>nb-Si; b,c,d) high-magnification SEM image of Sn<sup>#</sup>nb-Si and corresponding EDS mapping of elements Si and Sn for the zone; scales in c,d) are 500 nm; e) XRD patterns of evolution.

In Figure 1, scanning electron microscope (SEM) images of the samples show its morphological evolution. Figure 1d shows the SEM image of the AlSi alloy, with grains distributed homogeneously. Figure 1e shows that Al dissolves into Al<sup>3+</sup> with the addition of the HCl solution, resulting in the formation of nb-Si with the appearance of Si branches. The Si dendrites in the AlSi alloy form from the ultrahigh cooling rate, and they remain after dealloying, producing the branch-like appearance. Sn<sup>#</sup>nb-Si is synthesized after Sn nanospheres are deposited across the branches of nb-Si, producing the appearance of sabina chinensis with its fruit ball, as Figure 1f shows. Corresponding schematic diagrams are displayed to the left of the SEM images, in Figures 1a-1c. Figure 2a shows that the width of Sn<sup>#</sup>nb-Si particles is several (~5) micrometers. The mapping images in Figures 2b-2d reveal the element

distribution of Si and Sn. The result of EDS shows that the loading of Sn is 12.24% (wt%), which means that the content of Si is 87.76% (wt%). Three Sn “fruits” are outlined with circles in Figure 2d, while the red points of Si weaken in the same area. Smaller Sn fruits lay across the branches, which are not indicated specially. X-ray diffraction (XRD) patterns demonstrate the ingredient evolution of the samples (AlSi alloy, nb-Si and Sn<sup>#</sup>nb-Si). As Figure 2e shows, peaks of Al vanish after dealloying, meanwhile peaks of Si rise, and peaks of Sn occur after depositing. The disappearance/appearance of these characteristic peaks prove the etching of Al and depositing of Sn.

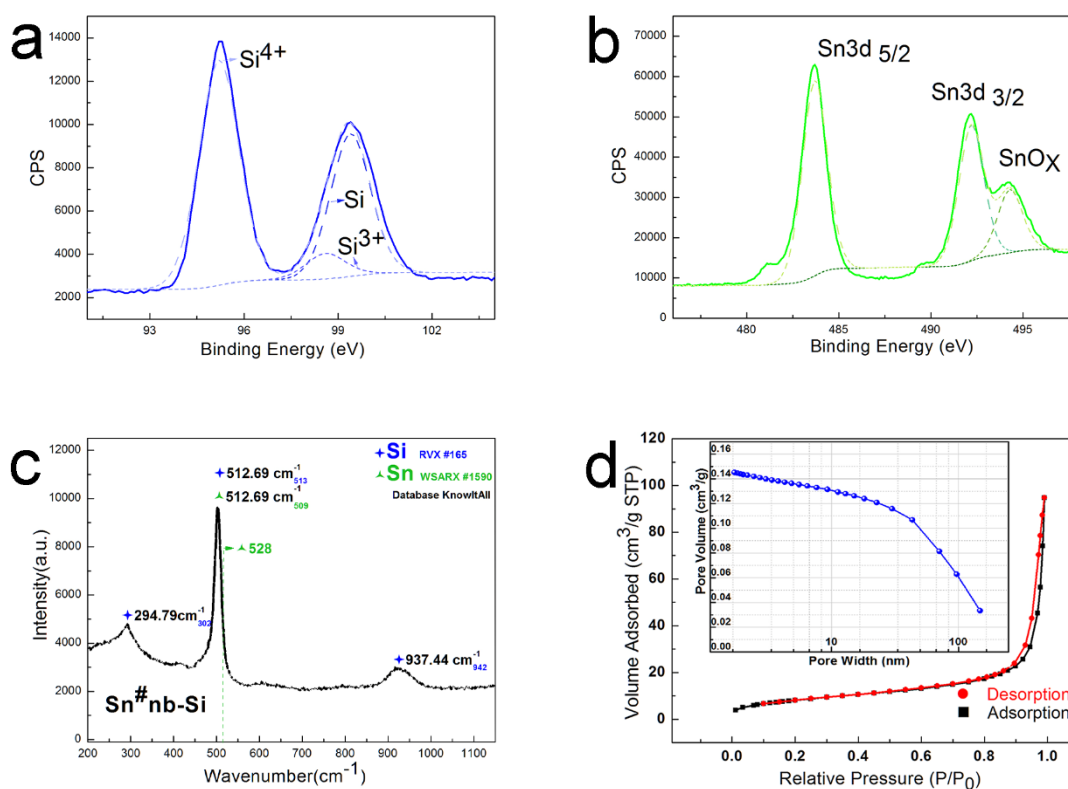


**Figure 3.** a,b) XPS spectra of Sn<sup>#</sup>nb-Si; c) Raman spectrum of Sn<sup>#</sup>nb-Si, subscript shows standard peak with blue (Si) and green (Sn), black shows the experimental results; d) nitrogen adsorption-desorption isotherms of Sn<sup>#</sup>nb-Si, inset is BJH adsorption cumulative pore volume (larger).

X-ray photo-electron spectroscope (XPS) results are listed in Figures 3a and 3b. The blue peak around 99.5 eV represents Si 2p 3/2, while the green peaks around 483 eV and 492 eV represent Sn 3d 5/2 and Sn 3d 3/2, respectively. The results of the XPS display the existence of both Si and Sn, showing the elemental composition of the samples. The Raman spectrum of Sn<sup>#</sup>nb-Si is shown in Figure 3c to present the element's information. As shown in the chart, Si and Sn manifest different bands due to their original ingredients. Peaks at 294.79 cm<sup>-1</sup> and 937.44 cm<sup>-1</sup> can be assigned to typical Raman mode of crystalline Si. Specifically, the peak at 512.69 cm<sup>-1</sup> is overlapped of Si and Sn due to standard peak of Si (513 cm<sup>-1</sup>) and Sn (509 cm<sup>-1</sup>), and the peak of Sn at 528 cm<sup>-1</sup> is low compared to the other two high

peaks.

Quantitative characterization of pore channels was tested by N<sub>2</sub> adsorption and desorption isotherms. The curve in Figure 3d displays a type IV adsorption/desorption isotherm with an H3-type hysteresis loop (based on IUPAC classification), confirming the existence of mesopores. The result, as shown by the curve, at relative pressure less than 0.1 suggests that a number of micropores work as a cave to store N<sub>2</sub> during process of adsorption/desorption. The specific surface area of Sn<sup>#</sup>nb-Si is assayed by the Brunauer-Emmett-Teller (BET) method, with a result of 30.42 m<sup>2</sup> g<sup>-1</sup>. As inset in Figure 3d, BJH gives the pore volume according to the variation of independent variable pore width, and the BJH adsorption cumulative surface area of pores between 1.7 nm and 300 nm width is 27.85 m<sup>2</sup> g<sup>-1</sup>.

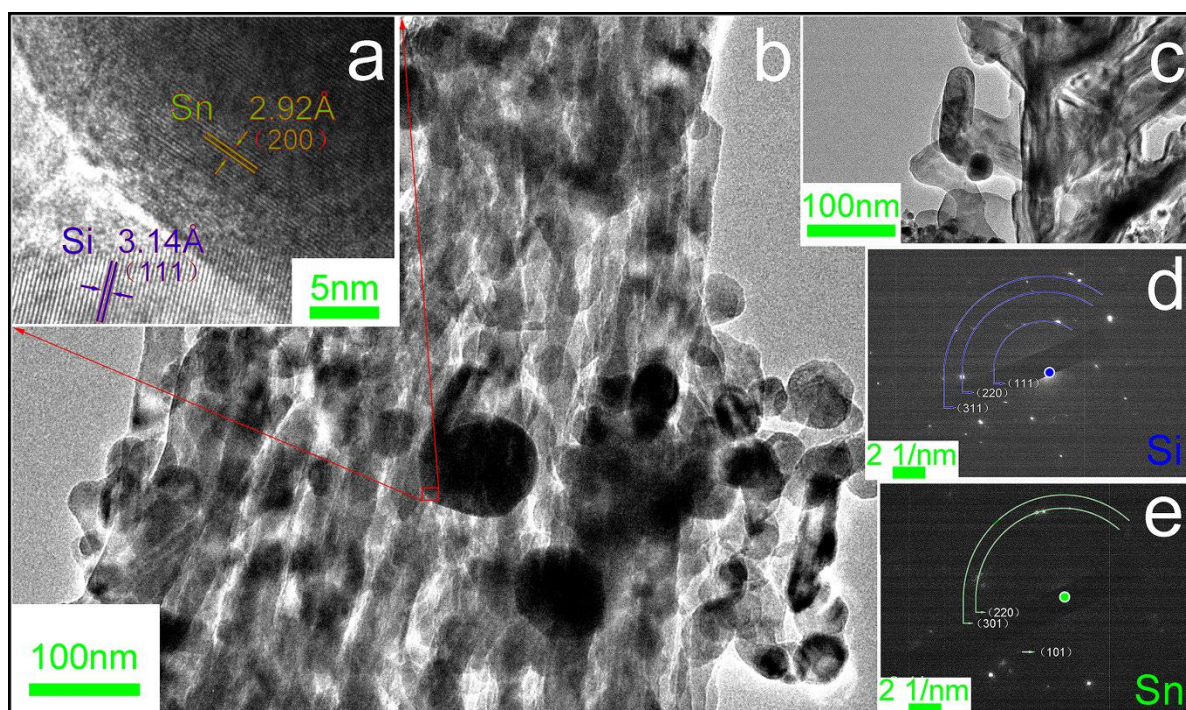


**Figure 4.** Results of TEM characterization of Sn<sup>#</sup>nb-Si. a) HRTEM image from selected zone; b,c) TEM images from another perspective; d,e) selected area electron diffraction (SAED) patterns of Si & Sn respectively.

Figure 4 shows the results of the transmission electron microscope (TEM) characterization of Sn<sup>#</sup>nb-Si. As can be seen in Figure 4b, Sn<sup>#</sup>nb-Si has an ordered ligament structure, looking like branches. Across the branches are the Sn nanospheres laying across the ligaments, and Figure 4c shows the morphology pinpointing another typical site. The high-resolution transmission electron microscope (HRTEM) image (Figure 4a) tells the interplanar crystal spacing of Si and Sn, 3.14 Å of crystallographic plane (111) and 2.92 Å of crystallographic plane (200), respectively, as previous studies have indicated[31,39]. According to the function,

$$d_{(hkl)} = \frac{a}{\sqrt{3}} \quad (1)$$

where  $a$  is lattice constant, we can know that the calculated  $d_{(111)}$  of Si is 3.136 Å, while  $d_{(200)}$  of Sn is 2.916 Å. The selected area electron diffraction (SAED) pattern of Sn<sup>#</sup>nb-Si shows rings of Si and Sn. Figure 4d shows crystal planes of (111), (220) and (311) of Si[29], while Figure 4e gives (220) and (301) of Sn[39], according to the results of XRD. In Figure 4e, the distance between the center spot and inner ring is measured to be 4.846 nm<sup>-1</sup>. In Ewald Sphere there is the function,

$$g_{hkl} = \frac{1}{d_{hkl}} \quad (2)$$

where  $d$  is interplanar crystal spacing. The calculated  $d_{hkl}$  is 2.064 nm of Sn, which is equal to 2.08 nm of plane (220). Other planes for Si and Sn can be calculated in the same way.

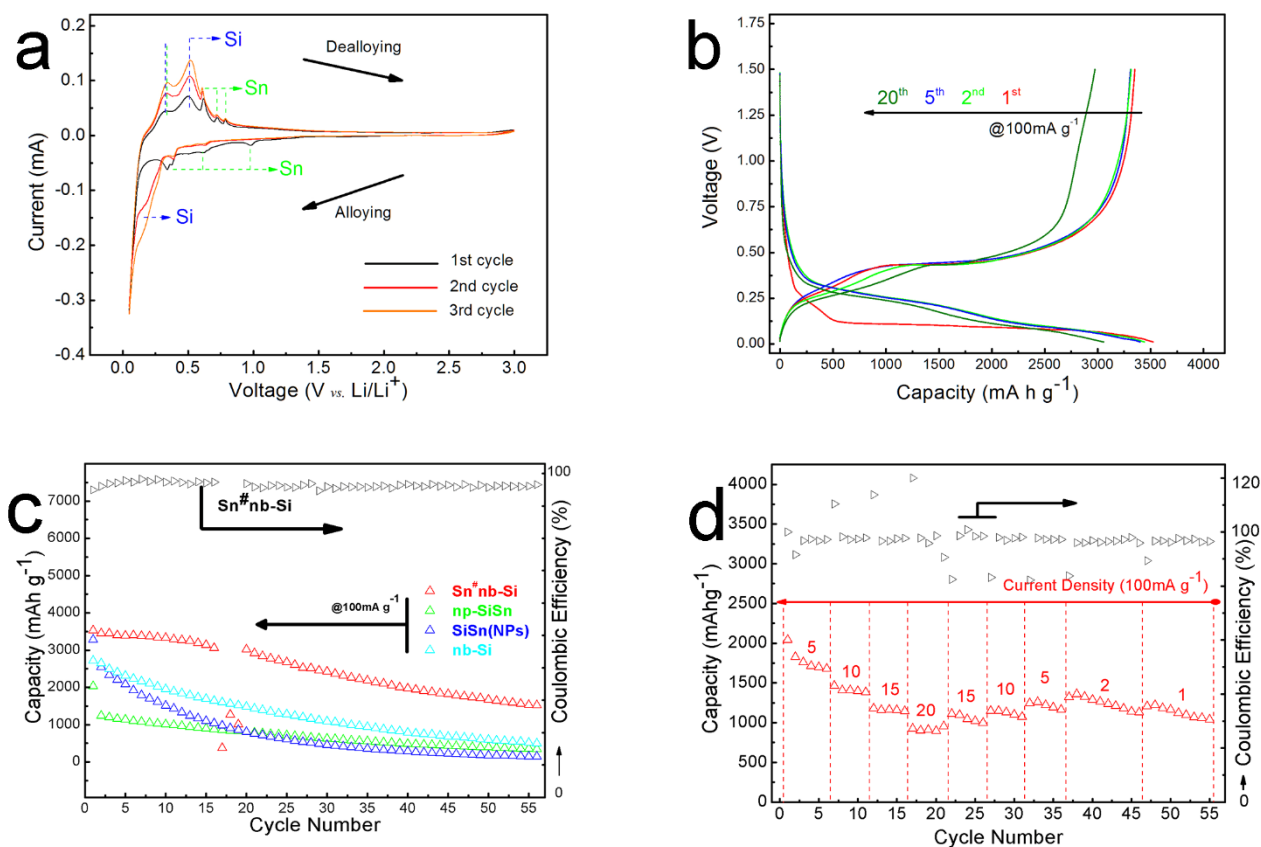


**Figure 5.** Electrochemical characterization of samples. **a)** Cyclic voltammetry curves of Sn<sup>#</sup>nb-Si at 0.1 mV s<sup>-1</sup> within 0.01-3 V versus Li<sup>+</sup>/Li; **b)** galvanostatic discharge-charge voltage profiles of Sn<sup>#</sup>nb-Si between 0.01-1.5 V at a current density of 100 mA g<sup>-1</sup>; **c)** cycling performance of Sn<sup>#</sup>nb-Si, np-SiSn, SiSn(NPs) and nb-Si electrodes at a current density of 100 mA g<sup>-1</sup>; **d)** rate capability of Sn<sup>#</sup>nb-Si anode at different current densities from 500 to 2000 mA g<sup>-1</sup>.

As shown in Figure 5a, cyclic voltammetry (CV) curves of Sn<sup>#</sup>nb-Si during its first three cycles display the typical peaks of Si and Sn, in the potential window of 0.01-3V (vs. Li<sup>+</sup>/Li) at a scan rate of 0.1 mV s<sup>-1</sup>. Alloying and dealloying processes take place clockwise; alloying equals lithiation and dealloying equals the opposite reaction. In the first cycle, characteristic peaks of Si and Sn arise constantly. Peaks at 0.34V, 0.62V and 0.979V show the alloying of Sn, with phase transition from Sn to

$\text{Li}_x\text{Sn}$ . Then, the end of the cathodic scan ( $\sim 0.1\text{V}$ ) shows the sharp peak of Si, indicating the formation of the  $\text{Li}_x\text{Si}$  alloy[40]. In an anodic scan, a peak at  $0.519\text{V}$  shows the dealloying of  $\text{Li}_x\text{Si}$ , and peaks at  $0.61\text{V}$ ,  $0.722\text{V}$  and  $0.788\text{V}$  show the same reaction of  $\text{Li}_x\text{Sn}$ . It should be noted that dealloying of  $\text{Li}_x\text{Si}$  and  $\text{Li}_x\text{Sn}$  occurs at the coinciding peak of  $0.346\text{V}$ .

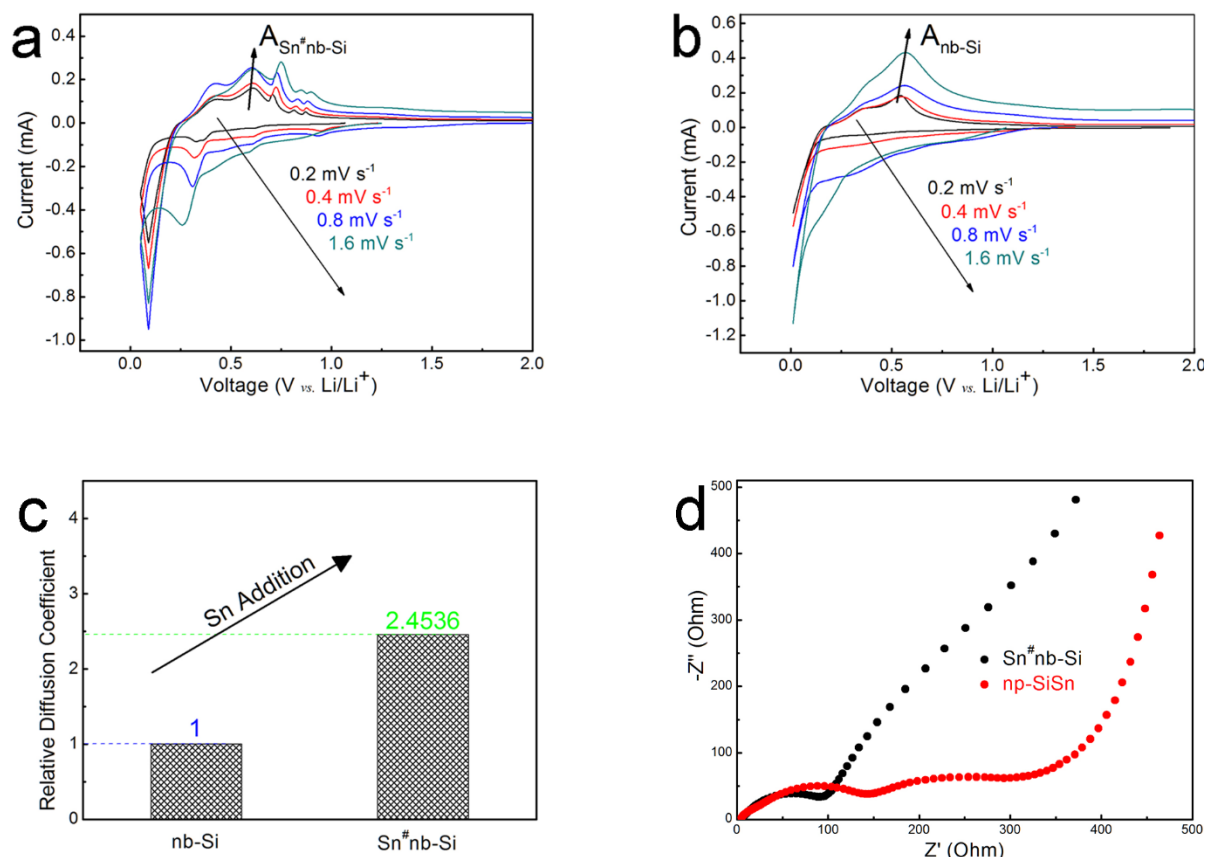


**Figure 6.** a,b) CV curves at scan rate from  $0.2$  to  $1.6\text{ mV s}^{-1}$ , respectively; c) relative diffusion coefficient, d) nyquist plots of  $\text{Sn}^\#\text{nb-Si}$  and  $\text{np-SiSn}$  anode after 90 cycles.

The ability of anodic peaks, compared to cathodic peaks, to shift to a higher potential is due to the polarization of electrodes. Subsequently, CV curves give an appearance of coinciding, suggesting a stable charging/discharging process and a relatively steady solid electrolyte interface (SEI), which forms mainly in the first cycle. Moreover, from the CV curves, it can be seen that the capacity above  $1.5\text{V}$  (vs.  $\text{Li}/\text{Li}^+$ ) contributes little to the total capacity. Figure 5b displays four charging/discharging profiles of half-cell with an  $\text{Sn}^\#\text{nb-Si}$  electrode at the current density of  $100\text{ mA g}^{-1}$  (voltage range of  $0.01\text{-}1.5\text{V}$ ). During the first discharging step, irreversible capacity is lost due to the formation of SEI. It is apparent that the first discharging platform is wider than the subsequent three ones, which corresponds to the sharp peak at  $\sim 0.1\text{V}$  in CV curves.

To characterize lithium the storage performance of  $\text{Sn}^\#\text{nb-Si}$  and control groups ( $\text{np-SiSn}$ , commercial Si & Sn nanoparticles (NPs-SiSn) and nb-Si), galvanostatic charge/discharge tests were conducted at room temperature. Figure 5c shows the results of the cycle performance of four cells at a

current density of 100 mA g<sup>-1</sup>. Sn<sup>#</sup>nb-Si demonstrates an excellent performance, possessing a reversible capacity of 1525.9 mA h g<sup>-1</sup> after 55 cycles; meanwhile, in the same condition, np-SiSn, NPs-SiSn and nb-Si possess 355.6 mA h g<sup>-1</sup>, 145.6 mA h g<sup>-1</sup>, 510.7 mA h g<sup>-1</sup>, respectively. NPs-SiSn powders are brittle and crack into chips during the insertion/desertion of Li<sup>+</sup>, resulting in the constant formation of SEI and the loss of capacity cyclically. The one-step method yields a nanoporous SiSn structure after dissolving Al from an AlSiSn alloy, but at the same time, Sn reacts with the HCl solution, destroying the ligaments of np-SiSn. The failure of nb-Si can be explained by a previous study which showed that the microstructure (i.e. nanobranches Si) is not the only decisive factor in improving cycle performance of the anode based on Si. Proper coatings may induce a compressive stress during lithiation, thereby limiting cracking[15]. Figure 5d demonstrates the rate performance of Sn<sup>#</sup>nb-Si, with a current density increasing from 500 mA g<sup>-1</sup> to 2000 mA g<sup>-1</sup>. After 20 cycles, reversible capacity at 2000 mA g<sup>-1</sup> still remains at 953.4 mA h g<sup>-1</sup>, showing that Sn<sup>#</sup>nb-Si yields a decent rate performance.

To further evaluate the influence of adding Sn, CV measurements at scan rates from 0.2 to 1.6 mV s<sup>-1</sup> were tested, as Figures 6a and 6b indicate. The relative ratio of the Li<sup>+</sup> diffusion coefficient of nb-Si to that of Sn<sup>#</sup>nb-Si can be determined by the Randles-Sevcik equation,

$$I_p = 2.69 \times 10^5 n^2 A D_{Li^+}^{1/2} v^{1/2} C_{Li^+} \quad (3)$$

where I<sub>p</sub> indicates the peak current, n is the number of electrons involved in the reaction, A is the apparent surface area of the electrode, v is the scan rate, and C<sub>Li<sup>+</sup></sub> is the concentration of Li<sup>+</sup>[41]. After a liner fitting of the first three plots, the relative diffusion coefficient is presented in Figure 6c, suggesting a 145% increase of Sn compared to nb-Si. After 10 cycles, the thickness of Sn<sup>#</sup>nb-Si electrode varied from 9.30 μm to 14.91 μm (increasing by 60.3%), as Figure 7f and 7h show. As for the NPs-SiSn electrode (Figure 7e and 7g), its thickness varied from 2.33 μm to 4.71 μm (increasing by 102.1%). After cycles, the electrochemical impedance spectroscopy (EIS) between Sn<sup>#</sup>nb-Si and np-SiSn was tested, investigating the kinetic mechanisms of Li<sup>+</sup> storage. As shown in Figure 6d, a depressed semicircle in a high-medium frequency range followed by an rising line in a low frequency range shows the result of EIS. It is known that a smaller semicircle radius of the alloy indicates relatively low charge transfer impedance. Sn<sup>#</sup>nb-Si possesses a narrower scale, indicating that Sn<sup>#</sup>nb-Si transfers Li<sup>+</sup> more efficiently than np-SiSn does. From the perspective of structural design, Sn<sup>#</sup>nb-Si has a stronger and more integrated network than np-SiSn, whose network is destroyed in the one-step method, showing powerful evidence to justify the superiority of Sn<sup>#</sup>nb-Si. Figure 7 shows the SEM images of electrodes before and after cycles. As shown in Figure 7c, active materials (NPs-SiSn) crack into pieces, while Sn<sup>#</sup>nb-Si (Figure 7d) shows a more robust framework, suggesting the stability of Sn<sup>#</sup>nb-Si during the process of lithiation and delithiation. From another perspective, the results from a cross-sectional view show that the morphology of Sn<sup>#</sup>nb-Si can efficiently buffer the volume expansion.

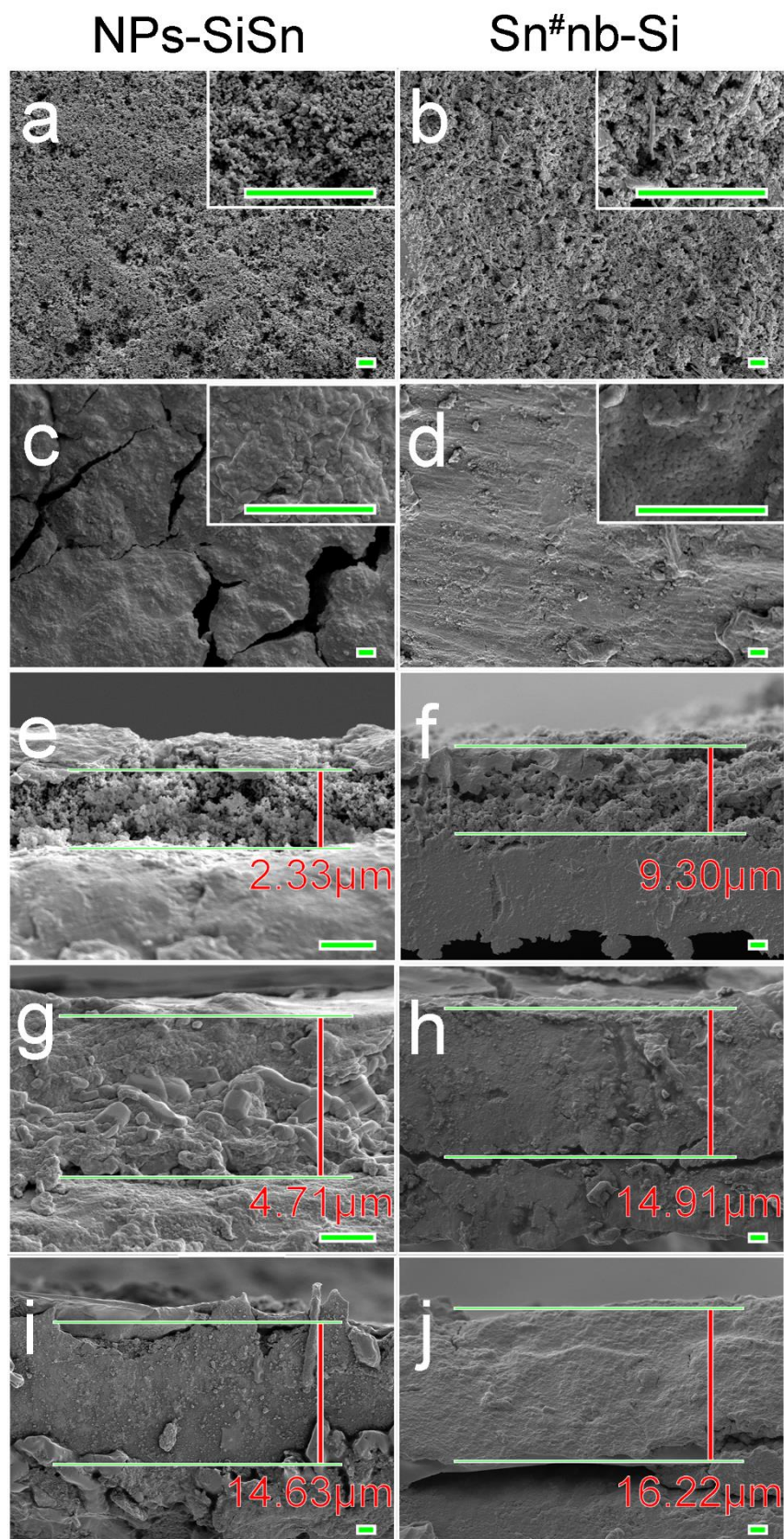


**Figure 7.** SEM images of electrode (NPs-SiSn and Sn<sup>#</sup>nb-Si) before and after cycles. (The scales in above figures are 1  $\mu\text{m}$ .) a,b) before cycles (top view); c,d) after 10 cycles (top view); e,f) before cycles (cross-sectional view), g,h) after 10 cycles (cross-sectional view), i,j) after 55 cycles (cross-sectional view).

Table 1 yields the comparison of lithium storage performance of similar materials discussed above. Accordingly, the impressive cycling performance of Sn<sup>#</sup>nb-Si can be attributed to the addition of Sn. Sn improves electronic conductivity and Li<sup>+</sup> diffusion between Si and the electrolyte, entailing rapid diffused speed and then a boosted cycle and rate performance. Furthermore, the structural design, i.e. the “fruit-branch” structure with integrated continuous ligaments, buffers the volume expansion, guaranteeing the integrity of the anode material. In addition, the harmonious distribution of pores (micro- and meso-) also plays an indispensable role in the process of lithiation/delithiation. The existence of pores increases the specific surface area, so that Li<sup>+</sup> can beat up and down effectively and react with active materials in a multi-site way.

**Table 1.** Comparison of lithium storage performance of similar materials.

Ref.	Materials	Current Density (mA g <sup>-1</sup> )	Capacity (mA h g <sup>-1</sup> )/Cycles
16	nanoporous silicon	200	2034/100
17	silicon nanowires	1.2 mA cm <sup>-2</sup>	4.2 mA h cm <sup>-2</sup>
18	Si NSs	100	441.7/40
10	DWSiNT	12C	600/6000
19	HPSi-Ag	100	~3000/30
3	N-PSi@C	7C	~1200/500
29	Si/RGO	100	1942/100
30	LiMg <sub>2</sub> Si	100	~450/20
31	3D-NPSiGe	1000	1158/150
32	np-Si <sub>15</sub> Sb <sub>15</sub>	100	647.4/90
33	Fe-Si/C		500/15
34	3Sn/Si NWs	0.1C	1865/100
35	Sn/Si NWs	100	1078/50
This work	Sn <sup>#</sup> nb-Si	100	1526/55

#### 4. CONCLUSION

In summary, through a process of dealloying followed by depositing, the Sn<sup>#</sup>nb-Si was successfully synthesized with an impressive performance. The two-step method delivers the integrity of ligaments, which produces the appearance of *sabina chinensis* with its fruit ball. The structural design at the nanoscale level ensures the tenacity of anode materials, assuring reversible capacity of the LIBs during the charging/discharging process. The synergistic effect from Si and Sn further supplies a high specific capacity and relatively high Li<sup>+</sup> conductivity rate, which presents 1525.9 mA h g<sup>-1</sup> at 100 mA g<sup>-1</sup>

<sup>1</sup> after 55 cycles and comparatively attractive rate performance. The combination of dealloying and depositing showcases an advanced way of synthesizing anode materials mildly and freely. In addition, the successful synthesis of Sn<sup>#</sup>nb-Si with its peculiar appearance and notable performance paves the way to advance the property of LIBs in the near future.

#### ACKNOWLEDGEMENTS

This work was supported by the National Natural Science Foundation of China (Grant no. 51571130).

#### References

1. J. Abe, K. Takahashi, K. Kawase, Y. Kobayashi and S. Shiratori, *ACS Applied Nano Materials*, 1 (2018) 2982.
2. P. Li, J. Y. Hwang and Y. K. Sun, *ACS nano*, 13 (2019) 2624.
3. B. Wang, J. Ryu, S. Choi, X. Zhang, D. Pribat, X. Li, L. Zhi, S. Park and R. S. Ruoff, *ACS nano*, 13 (2019) 2307.
4. H. Zhang, P. Zong, M. Chen, H. Jin, Y. Bai, S. Li, F. Ma, H. Xu and K. Lian, *ACS nano*, 13 (2019) 3054.
5. X. Yao, G. Guo, P. Z. Li, Z. Z. Luo, Q. Yan and Y. Zhao, *ACS applied materials & interfaces*, 9 (2017) 42438.
6. L. Li, Z. Li, A. Yoshimura, C. Sun, T. Wang, Y. Chen, Z. Chen, A. Littlejohn, Y. Xiang, P. Hundekar, S. F. Bartolucci, J. Shi, S. F. Shi, V. Meunier, G. C. Wang and N. Koratkar, *Nature communications*, 10 (2019) 1764.
7. L. Kong, Y. Wang, H. Yu, B. Liu, S. Qi, D. Wu, W. H. Zhong, G. Tian and J. Wang, *ACS applied materials & interfaces*, 11 (2019) 2978.
8. F. Huang, Y. Xu, B. Peng, Y. Su, F. Jiang, Y.-L. Hsieh and Q. Wei, *ACS Sustainable Chemistry & Engineering*, 3 (2015) 932.
9. Q. Li, S. Jiao, L. Luo, M. S. Ding, J. Zheng, S. S. Cartmell, C. M. Wang, K. Xu, J. G. Zhang and W. Xu, *ACS applied materials & interfaces*, 9 (2017) 18826.
10. H. Wu, G. Chan, J. W. Choi, I. Ryu, Y. Yao, M. T. McDowell, S. W. Lee, A. Jackson, Y. Yang, L. Hu and Y. Cui, *Nat Nanotechnol*, 7 (2012) 310.
11. W. Lv, Z. Wang, H. Cao, Y. Sun, Y. Zhang and Z. Sun, *ACS Sustainable Chemistry & Engineering*, 6 (2018) 1504.
12. K. Feng, M. Li, W. Liu, A. G. Kashkooli, X. Xiao, M. Cai and Z. Chen, *Small*, 14 (2018) 1702737.
13. X. Liu, H. Zheng, L. Zhong, S. Huang, K. Karki, L. Zhang, and J. Cho, *Nano letters*, 11 (2011) 3312.
14. T. D. Bogart, X. Lu, M. Gu, C. Wang and B. A. Korgel, *RSC Adv.*, 4 (2014) 42022.
15. N.-S. Choi, Y. Yao, Y. Cui and J. Cho, *Journal of Materials Chemistry*, 21 (2011) 9825.
16. Y. An, H. Fei, G. Zeng, L. Ci, S. Xiong, J. Feng and Y. Qian, *ACS nano*, 12 (2018) 4993.
17. H. T. Nguyen, F. Yao, M. R. Zamfir, C. Biswas, K. P. So, Y. H. Lee, S. M. Kim, S. N. Cha, J. M. Kim and D. Pribat, *Advanced Energy Materials*, 1 (2011) 1154.
18. X. Yu, F. Xue, H. Huang, C. Liu, J. Yu, Y. Sun, X. Dong, G. Cao and Y. Jung, *Nanoscale*, 6 (2014) 6860.
19. D. Chen, X. Mei, G. Ji, M. Lu, J. Xie, J. Lu and J. Y. Lee, *Angewandte Chemie*, 51 (2012) 2409.
20. X. Zhang, D. Kong, X. Li and L. Zhi, *Advanced Functional Materials*, 29 (2019) 1806061.
21. W. Lu, X. Guo, Y. Luo, Q. Li, R. Zhu and H. Pang, *Chemical Engineering Journal*, 355 (2019) 208.
22. G. Li, B. Huang, Z. Pan, X. Su, Z. Shao and L. An, *Energy & Environmental Science*, 12 (2019)

2030.

23. J. Henschel, J. L. Schwarz, F. Glorius, M. Winter and S. Nowak, *Anal Chem*, 91 (2019) 3980.
24. W. An, B. Gao, S. Mei, B. Xiang, J. Fu, L. Wang, Q. Zhang, P. K. Chu and K. Huo, *Nature communications*, 10 (2019) 1447.
25. W. Qi, J. G. Shapter, Q. Wu, T. Yin, G. Gao and D. Cui, *Journal of Materials Chemistry A*, 5 (2017) 19521.
26. S. Liu, J. Feng, X. Bian, Y. Qian, J. Liu and H. Xu, *Nano Energy*, 13 (2015) 651.
27. S. Liu, J. Feng, X. Bian, J. Liu and H. Xu, *Energy & Environmental Science*, 9 (2016) 1229.
28. W. Li, X. Sun and Y. Yu, *Small Methods*, 1 (2017) 1600037.
29. J. Feng, Z. Zhang, L. Ci, W. Zhai, Q. Ai and S. Xiong, *Journal of Power Sources*, 287 (2015) 177.
30. R. Ma, Y. Liu, Y. Yang, M. Gao and H. Pan, *Applied Physics Letters*, 105 (2014) 213901.
31. Y. Yang, S. Liu, X. Bian, J. Feng, Y. An and C. Yuan, *ACS nano*, 12 (2018) 2900.
32. C. Yuan, S. Liu, Y. Yang, M. Yu, Y. Tian, J. Wang and X. Bian, *ChemElectroChem*, 5 (2018) 3809.
33. H. Dong, R. X. Feng, X. P. Ai, Y. L. Cao and H. X. Yang, *Electrochimica Acta*, 49 (2004) 5217.
34. A. Kohandehghan, K. Cui, M. Kupsta, E. Memarzadeh, P. Kalisvaart and D. Mitlin, *Journal of Materials Chemistry A*, 2 (2014) 11261.
35. E. Mullane, T. Kennedy, H. Geaney, C. Dickinson and K. M. Ryan, *Chemistry of Materials*, 25 (2013) 1816.
36. Y. Yuan, W. Xiao, Z. Wang, D. J. Fray and X. Jin, *Angewandte Chemie*, 57 (2018) 15743.
37. X. Li, X. Meng, J. Liu, D. Geng, Y. Zhang, M. N. Banis, Y. Li, J. Yang, R. Li, X. Sun, M. Cai and M. W. Verbrugge, *Advanced Functional Materials*, 22 (2012) 1647.
38. M. Nisula and M. Karppinen, *Nano letters*, 16 (2016) 1276.
39. S. Fan, L. Y. Lim, Y. Y. Tay, S. S. Pramana, X. Rui, M. K. Samani, Q. Yan, B. K. Tay, M. F. Toney and H. H. Hng, *Journal of Materials Chemistry A*, 1 (2013) 14577.
40. D. Ma, Z. Cao and A. Hu, *Nano-micro letters*, 6 (2014) 347.
41. Y. Hu, W. Chen, T. Lei, B. Zhou, Y. Jiao, Y. Yan, X. Du, J. Huang, C. Wu, X. Wang, Y. Wang, B. Chen, J. Xu, C. Wang and J. Xiong, *Advanced Energy Materials*, 9 (2019) 1802955.

© 2020 The Authors. Published by ESG ([www.electrochemsci.org](http://www.electrochemsci.org)). This article is an open access article distributed under the terms and conditions of the Creative Commons Attribution license (<http://creativecommons.org/licenses/by/4.0/>).